

## First-principles study of water adsorption monolayer on Pt(111): Adsorption energy and second-order nonlinear susceptibility

Jun Haruyama <sup>1,\*</sup>, Toshiki Sugimoto <sup>2,3</sup> and Osamu Sugino <sup>1</sup>

<sup>1</sup>The Institute for Solid State Physics, The University of Tokyo, 5-1-5 Kashiwanoha, Kashiwa, Chiba 277-8581, Japan

<sup>2</sup>Department of Materials Molecular Science, Institute for Molecular Science, Myodaiji, Okazaki, Aichi 444-8585, Japan

<sup>3</sup>Precursory Research for Embryonic Science and Technology, Japan Science and Technology Agency, Saitama 332-0012, Japan



(Received 26 February 2023; revised 15 May 2023; accepted 31 October 2023; published 29 November 2023)

To establish first-principles calculation accuracy and methodology for a metal/water interface, we investigated the H<sub>2</sub>O adsorption monolayer on a Pt(111) surface and developed a density functional theory (DFT)-based method for analyzing the second-order nonlinear susceptibility  $\chi_{zzz}^{(2)}$ . The H<sub>2</sub>O adsorption structures of  $\sqrt{3} \times \sqrt{3}$  with H-up/H-down models,  $\sqrt{39} \times \sqrt{39}$  with a six-member ring model,  $\sqrt{39} \times \sqrt{39}$ , and  $\sqrt{37} \times \sqrt{37}$  with five- and seven-member ring models were considered by applying DFT calculations. The last two structures were found to be the most stable, and their heats of adsorption, including zero-point vibration correction, were in good agreement with the activation energy of desorption in the experiment with the vdW-DF2-B86R functional. Furthermore, by employing the density functional perturbation formulation combined with the effective-screening medium (ESM) + a finite electric field approach, we obtained the second-order nonlinear susceptibility  $\chi_{zzz}^{(2)}$  of the  $\sqrt{39}$  and  $\sqrt{37}$  5–7-ring structures. The negative and positive signs of  $\text{Im} \chi_{zzz}^{(2)}$  in the high (3000–3500 cm<sup>-1</sup>) and low (600–2400 cm<sup>-1</sup>) frequency regions, respectively, were obtained. The spectra show negative double peaks in the high-frequency region, consistent with those obtained by heterodyne-detected sum frequency generation spectroscopy. This study provides a fundamental basis for improving our understanding of H<sub>2</sub>O adsorption on metal surfaces.

DOI: [10.1103/PhysRevMaterials.7.115803](https://doi.org/10.1103/PhysRevMaterials.7.115803)

### I. INTRODUCTION

In electrochemistry, a charge-transfer reaction occurs at the interface between a metal electrode and an electrolyte solution [1,2]. In particular, the metal/water interface is of general importance and continued interest [3], because aqueous solutions are often utilized for energy conversion devices such as fuel cells or water electrolysis systems. Thus, it is useful to understand and predict the properties of H<sub>2</sub>O molecules on a metal surface to improve the performance of such devices [4,5]. In addition, the conversion efficiency of an electrochemical reaction depends on the free-energy landscape [6] of its rate-determining step, such as the oxygen reduction reaction. Then an accurate description of the interactions between water–water, electrolyte–water, and metal surface–water is essential to estimate the free energy of reaction intermediate states. In this study we focus on the metal–water interaction and select a fundamental system: H<sub>2</sub>O adsorption on a Pt(111) surface.

Growth of an epitaxial structure with adsorbed H<sub>2</sub>O molecules and crystalline ice film has been observed on a Pt(111) surface at low temperatures [7]. A variety of surface science techniques, such as He-atom scattering (HAS), low-energy electron diffraction (LEED), temperature-programmed desorption (TPD), scanning tunneling microscopy (STM), infrared reflection adsorption spectroscopy (IRAS), and first-principles density functional theory (DFT) calculations

have been applied to investigate the Pt(111)/H<sub>2</sub>O structure [8–10].

In 1997, Glebov *et al.* showed the formation of a well-ordered H<sub>2</sub>O overlayer on Pt(111) surface with ( $\sqrt{37} \times \sqrt{37}$ )R25.3° or ( $\sqrt{39} \times \sqrt{39}$ )R16.1° symmetry by HAS diffraction patterns [11]. They suggested possible lateral arrangements of H<sub>2</sub>O molecules commensurate with the  $\sqrt{37}$  and  $\sqrt{39}$  supercells, in which the hydrogen bonds construct six-member rings. Haq *et al.* also observed a ( $\sqrt{39} \times \sqrt{39}$ )R16.1° LEED pattern on the first layer of H<sub>2</sub>O molecules on Pt(111) [12]. They also investigated the activation energy of desorption  $E_a$  for the H<sub>2</sub>O layers on Pt(111) by TPD analysis, which showed  $E_a = 52 \pm 2$  kJ/mol [12]. However, the experimental condition of TPD is not isothermal, and the activation energy from TPD analysis contains some errors. After that, Daschbach *et al.* measured the desorption rates of the H<sub>2</sub>O layers on Pt(111) by HAS under isothermal conditions and a more accurate estimation by an Arrhenius plot ( $E_a = 54.2 \pm 3$  kJ/mol) [13].

In 2010, Nie *et al.* observed triangular depression STM images on the H<sub>2</sub>O first layer and proposed that the triangle represents a hexagon of H<sub>2</sub>O molecules surrounding five- and seven-member rings [14,15]. In a subsequent study, Feibelman *et al.* assigned low-frequency modes (ca. 2000 cm<sup>-1</sup>) observed by IRAS on the H<sub>2</sub>O monolayer to redshifted OH-stretch modes, which come from six anomalously short O–O distances (2.5–2.6 Å) per  $\sqrt{37}$  and  $\sqrt{39}$  supercells, predicted by DFT calculations [16]. From the consistency between the experimental observation and the theoretical calculations, the

\*Corresponding author: haruyama@issp.u-tokyo.ac.jp

structure suggested by Nie *et al.* can be considered thermodynamically stable at low temperatures. The detailed structure and activation energy of desorption can be obtained, and the H<sub>2</sub>O adsorption monolayer on Pt(111) can be considered an ideal system for discussing the accuracy of first-principles calculations.

In these applications, sum frequency generation (SFG) vibrational spectroscopy has become an advanced method for determining the configuration of H<sub>2</sub>O on a metal surface. In 1998, Su *et al.* observed SFG spectra at OH-stretch resonances as a function of ice film thickness on Pt(111) [17]. Because the SFG spectral is proportional to the square amplitude of second-order nonlinear susceptibility and is allowed only in a medium without inversion symmetry, they discussed that the enhancement suggests the polar ordering of H<sub>2</sub>O molecules in the films. Recently, the ice film structure was further investigated using heterodyne-detected SFG spectroscopy, which can obtain the imaginary part of the second-order nonlinear susceptibility,  $\text{Im } \chi^{(2)}$ . Because a positive/negative sign of  $\text{Im } \chi^{(2)}$  corresponds to the H-up/H-down structure of surface H<sub>2</sub>O molecules,  $\text{Im } \chi^{(2)}$  spectra observed by Sugimoto *et al.* in 2016 clarified that an H-down oriented structure on Pt(111) is formed from the first layer to hundreds of layers [18]. In contrast,  $\text{Im } \chi^{(2)}$  signals on Rh(111) indicated that adsorbed H<sub>2</sub>O molecules take a mixture of H-down and H-up configurations, namely, crystalline films with disordered H orientations [19]. Thus, second-order nonlinear susceptibility  $\chi^{(2)}$  is helpful in determining the configuration of H<sub>2</sub>O adsorption layers [10]. For further quantitative comparisons between theory and experiment, it is desirable to calculate  $\chi^{(2)}$  using the first-principles method.

In this study we used DFT calculations to investigate the most stable structure for H<sub>2</sub>O adsorption on Pt(111), and we calculated the adsorption energies of several model structures with  $\sqrt{39}$  and  $\sqrt{37}$  cells. In addition, the zero-point vibration energies of stable structures were considered. We discuss the prediction accuracy of the DFT calculations by comparing the corrected adsorption energies with the activation energy of desorption in an experiment, assuming that the H<sub>2</sub>O adsorption process can be described as typical physisorption. We further developed a practical approach to treat metal/adsorbate systems using first-principles calculations and evaluated the vibrational responses, namely, infrared (IR) and Raman intensity, and second-order nonlinear susceptibility  $\chi^{(2)}$  for stable structures. We compared them with those obtained in experiments; in particular, the imaginary part of  $\chi^{(2)}$  should be comparable to that obtained by heterodyne-detected SFG spectroscopy [18].

This paper is organized as follows: Section II A describes the previous DFT calculations of the ice Ih phase and H<sub>2</sub>O adsorption on Pt(111). The heat of sublimation in ice Ih and the adsorption energy of one H<sub>2</sub>O molecule on Pt(111) are also provided. Section II B presents the structure of the H<sub>2</sub>O adsorption monolayer used in this study. Section II C describes the calculation method for second-order nonlinear susceptibility within the DFT calculations. Section II D lists the computational details. Section III A provides the results for the adsorption energies, pair distribution functions, and heats of adsorption. Section III B provides the results of the

IR and Raman intensity and second-order nonlinear susceptibility. Finally, Sec. IV presents the conclusions.

## II. METHODS AND MODELS

### A. DFT calculations of crystalline ice and adsorbed H<sub>2</sub>O monomer

Electronic structure calculations based on DFT, represented as an applied exchange–correlation density functional, have become a state-of-the-art method for predicting adsorption structures and properties in surface science. However, the quantitative description of the interaction between H<sub>2</sub>O molecules, that is, hydrogen bonding, remains problematic for the proposed functionals. Using the Bernal–Fowler periodic model of the ice Ih phase, Hamann reported the lattice energies obtained by some density functionals in 1998 [20]. In subsequent studies it was shown that common generalized gradient approximation functionals gave large lattice energies compared with a reference value (the errors were approximately 50–100 meV/H<sub>2</sub>O). In contrast, van der Waals (vdW) type functionals, in which a nonlocal correlation term accurately describes intermolecular interactions, gave closer lattice energies (the errors were within 20 meV/H<sub>2</sub>O) [21,22].

For the discussion of functional accuracies, we evaluated the lattice energy  $E_{\text{lat}}$ , zero-point vibration correction  $\Delta E_{\text{ZPE}}$ , and heat of sublimation  $H_{\text{sub}}$  of ice Ih from Eqs. (S1)–(S3) in the Supplemental Material (SM) [23]. The computational details are described in Sec. S1 [23]. The calculated values using the Perdew–Burke–Ernzerhof (PBE) [26], vdW-DF [27], and vdW-DF2-B86R [28] functionals are listed in Table S1 [23]. The lattice parameters and energies of PBE and vdW-DF are consistent with those of previous DFT studies [21,22]. All functionals estimated almost the same  $\Delta E_{\text{ZPE}}$ ; the zero-point energy in ice Ih is not sensitive to these functionals. Compared with the heat of sublimation in the thermochemical data ( $H_{\text{sub}} = 491$  meV/H<sub>2</sub>O at 0 K) [29], PBE and vdW-DF overestimated and underestimated it, respectively. In addition, vdW-DF2-B86R overestimated the lattice energy and heat of sublimation by approximately 100 meV. However, these estimated accuracies of the H<sub>2</sub>O–H<sub>2</sub>O interaction cannot be invoked for the Pt–H<sub>2</sub>O interaction, because vdW-DF2-B86R is considered to be the best choice among the three functionals for describing the properties of the H<sub>2</sub>O adsorption monolayer on Pt(111).

In addition to the H<sub>2</sub>O–H<sub>2</sub>O interaction, it is also ambiguous whether the metal–H<sub>2</sub>O interaction can be correctly described by DFT calculations. For physisorbed H<sub>2</sub>O molecules on the Rh(111) surface, Hamada *et al.* showed that the interaction energies of Rh–H<sub>2</sub>O by PBE and vdW-DF are small and comparable, respectively, compared with those of H<sub>2</sub>O–H<sub>2</sub>O in ice Ih [30]. Carrasco *et al.* reported that some functionals predicted that H<sub>2</sub>O adsorption layers on metal surfaces are thermodynamically unstable, although the wetting layers have been well characterized experimentally [31]. They suggested that nonlocal correlations included in advanced vdW functionals influence the relative stabilities of wetting H<sub>2</sub>O layers on metal surfaces and bulk ice [31,32].

Here, considering the adsorption of one H<sub>2</sub>O molecule on Pt(111), the difference in Pt–H<sub>2</sub>O interactions obtained by

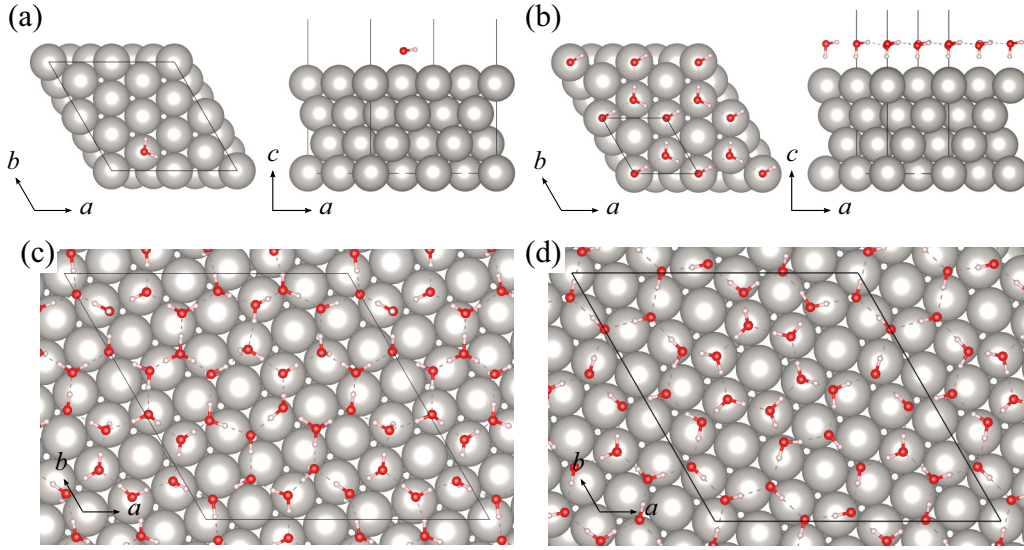


FIG. 1. Structures of  $\text{H}_2\text{O}$  adsorption monolayer on Pt(111) surface supercells: (a) one H-para molecule in  $2\sqrt{3} \times 2\sqrt{3}$  cell, (b)  $\sqrt{3}$  H-down, (c)  $\sqrt{39}$  6-ring, and (d)  $\sqrt{39}$  5-7-ring. The Pt, O, and H atoms are shown as gray, red, and white circles, respectively.

the selected functionals is discussed. The adsorption energy  $E_{\text{ad}}$  is defined using the DFT total energy  $E_{\text{DFT}}$ :

$$E_{\text{ad}} = -\{E_{\text{DFT}}(\text{Pt}/n\text{H}_2\text{O}) - E_{\text{DFT}}(\text{Pt}) - nE_{\text{DFT}}(\text{H}_2\text{O})\}/n, \quad (1)$$

where  $\text{Pt}/n\text{H}_2\text{O}$ ,  $\text{Pt}$ , and  $\text{H}_2\text{O}$  represent the systems of  $n\text{H}_2\text{O}$  adsorption on the Pt(111), pristine Pt(111) surface, and an isolated  $\text{H}_2\text{O}$  molecule, respectively. According to this definition, larger adsorption energy leads to a more stable structure. We conducted DFT calculations and evaluated  $E_{\text{ad}}$  of one  $\text{H}_2\text{O}$  molecule. The adsorption structure is shown in Fig. 1(a), and the computational details are described in Sec. II D. The results of  $E_{\text{ad}}$  and the interatomic distances between the Pt and O atoms  $d_{\text{Pt-O}}$  are listed in Table I. The adsorption energy obtained by vdW-DF2-B86R was approximately twice that obtained by the other two functionals. The interatomic distances are discussed in comparison with monolayer  $\text{H}_2\text{O}$  on Pt(111) in Sec. III A.

### B. $\text{H}_2\text{O}$ adsorption monolayer structures

An ordered  $\text{H}_2\text{O}$  layer on Pt(111) with  $(\sqrt{3} \times \sqrt{3})R30^\circ$  symmetry is a basic model for investigating  $\text{H}_2\text{O}$  adsorption. In 2004, Meng *et al.* conducted DFT calculations of the ordered layer with different H-up/H-down configurations on various metal surfaces [33]. They also considered the supercell ( $\sqrt{37}$  and  $\sqrt{39}$ ) model with a six-ring on Pt(111),

TABLE I. Adsorption energies  $E_{\text{ad}}$  and interatomic distances  $d_{\text{Pt-O}}$  of one  $\text{H}_2\text{O}$  molecule on Pt(111) calculated by three DFT functionals.

Functional	$E_{\text{ad}}$ (meV)	$d_{\text{Pt-O}}$ ( $\text{\AA}$ )
PBE	225	2.45
vdW-DF	253	2.71
vdW-DF2-B86R	423	2.37

suggested by Glevob *et al.* [11] and Feibelman *et al.* [34], and concluded that Glevob's model is more stable than the conventional  $\sqrt{3}$  model [33]. Following that study, we treated the H-up/H-down structures with a  $\sqrt{3}$  cell (represented as  $\sqrt{3}$  H-up/H-down), and the six-ring model consists of 32  $\text{H}_2\text{O}$  molecules in a  $\sqrt{39}$  cell ( $\sqrt{39}$  6-ring) as shown in Figs. 1(b) and 1(c), respectively. We introduced a small amount of dissociated  $\text{H}_2\text{O}$  molecules, that is,  $\text{H}_3\text{O}$  and  $\text{OH}$ , into the  $\sqrt{39}$  six-ring model and evaluated  $E_{\text{ad}}$  by optimizing several structures with some combinations of dissociated  $\text{H}_2\text{O}$  and H-up/H-down orientations. We further considered the adsorption model with five- and seven-member rings proposed by Nie *et al.* consisting of 28  $\text{H}_2\text{O}$  molecules in a  $\sqrt{39}$  cell ( $\sqrt{39}$  5-7-ring) as shown in Fig. 1(d). Almost the same structure consisting of 26  $\text{H}_2\text{O}$  in a  $\sqrt{37}$  cell ( $\sqrt{37}$  5-7-ring) was also considered.

For selected adsorption structures, we evaluated the zero-point vibrational correction  $\Delta E_{\text{ZPE}}$  and the heat of adsorption  $H_{\text{ad}}$ , defined as

$$\Delta E_{\text{ZPE}} = -\{E_{\text{ZPE}}(\text{Pt}/n\text{H}_2\text{O}) - E_{\text{ZPE}}(\text{Pt}) - nE_{\text{ZPE}}(\text{H}_2\text{O})\}/n, \quad (2)$$

$$H_{\text{ad}} = E_{\text{ad}} + \Delta E_{\text{ZPE}}. \quad (3)$$

The zero-point vibrational energy  $E_{\text{ZPE}}$  within the harmonic approximation is evaluated by the summation of the vibrational (phonon) eigenfrequencies  $\omega_v$ :

$$E_{\text{ZPE}} = \frac{1}{2} \sum_v \hbar\omega_v \text{ or } \frac{1}{2} \int \hbar\omega g(\omega) d\omega, \quad (4)$$

where  $\hbar$  and  $g(\omega)$  are the Planck constant over  $2\pi$  and the density of states (DOS) of vibrational (phonon) modes, respectively. Finite-temperature vibrational contributions are ignored in this study, because the contributions estimated by the independent harmonic oscillator approximation [35] were negligibly small compared with  $\Delta E_{\text{ZPE}}$  at typical spectroscopic temperature, see Sec. S2 [23].

### C. Second-order nonlinear susceptibility

The second-order nonlinear susceptibility  $\chi^{(2)}$  represents the second-order response of the macroscopic polarization  $\mathbf{P}$  under an external electric field  $\mathbf{E}$ . When two fields enter a polarizable medium,  $\mathbf{E}(\omega_{\text{IR}})$  and  $\mathbf{E}(\omega_{\text{vis}})$ , the frequencies of which belong to the IR and visible regions, the second-order term generates macroscopic polarization oscillating with the sum of the two frequencies:  $\mathbf{P}(\omega_{\text{SFG}} = \omega_{\text{IR}} + \omega_{\text{vis}})$ , resulting in SFG signals with an intensity proportional to  $|\mathbf{P}|^2$ . Considering the sum-over-states representation of  $\chi^{(2)}$  derived from the perturbation theory and SFG experimental conditions ( $\omega_{\text{IR}} \ll \omega_{\text{vis}}$  and  $\omega_{\text{vis}}$  is far from the electronic transition energies of adsorbate molecules),  $\chi^{(2)}$  can be approximated by an IR resonant frequency term only [36–39]:

$$\chi_{\alpha\beta\gamma}^{(2)}(\omega_{\text{IR}}) = \sum_{\nu} \frac{A_{\alpha\beta\gamma,\nu}}{\omega_{\nu} - \omega_{\text{IR}} - i\Gamma_{\nu}}, \quad (5)$$

where  $\omega_{\nu}$  and  $\Gamma_{\nu}$  represent the vibrational (phonon) frequency of the eigenmode  $\nu$  and the corresponding dephasing rate, respectively. In principle,  $\Gamma_{\nu}$  can be estimated by phonon-phonon or electron-phonon coupling constants; however, this study treats  $\Gamma_{\nu}$  as phenomenological parameters. The subscripts  $\alpha$ ,  $\beta$ , and  $\gamma$  represent directions. The other resonant and nonresonant terms are ignored in this study. The numerator  $A_{\alpha\beta\gamma,\nu}$  is composed of the transition matrix elements between vibrational eigenmodes  $|0\rangle$  and  $|\nu\rangle$  with respect to the polarizability and dipole moment:  $\langle 0|\hat{\alpha}_{\alpha\beta}|\nu\rangle \times \langle \nu|\hat{\mu}_{\gamma}|0\rangle$  ( $\hat{\alpha}_{\alpha\beta}$  and  $\hat{\mu}_{\gamma}$  are the operators of the polarizability tensor and dipole moment, respectively).

Using the density functional perturbation theory (DFPT) [40,41] within the harmonic approximation, the numerator can be represented as

$$A_{\alpha\beta\gamma,\nu} = \langle 0|\hat{\alpha}_{\alpha\beta}|\nu\rangle \times \langle \nu|\hat{\mu}_{\gamma}|0\rangle = \left( \sum_{\kappa,\gamma'} R_{\kappa,\alpha\beta\gamma'} U_{\nu,\mathbf{q}=0}(\kappa,\gamma') \right) \times \left( \sum_{\kappa,\gamma'} Z_{\kappa,\gamma\gamma'}^* U_{\nu,\mathbf{q}=0}(\kappa,\gamma') \right), \quad (6)$$

where  $U_{\nu,\mathbf{q}=0}(\kappa,\alpha)$ ,  $Z_{\kappa,\alpha\beta}^*$ , and  $R_{\kappa,\alpha\beta\gamma}$  represent the displacements of vibrational (phonon) eigenmodes at reciprocal space  $\mathbf{q} = 0$ , the Born effective charge tensor [40], and the Raman tensor [42] (a third-rank tensor related to the Raman process [43,44]) on an atom index  $\kappa$ . The notations conformed to the previous study [40]. Because the first and second components of Eq. (6) are interpreted as the related Raman and IR components, respectively, the Raman- and IR-active vibrational (phonon) modes only contribute to the second-order nonlinear susceptibility  $\chi^{(2)}$ , which is discussed in Sec. III B. In addition, decoupled molecular treatment has been widely applied to evaluate the second-order nonlinear susceptibility  $\chi^{(2)}$  in experimental analyses and theoretical studies [36–39,45–47]; however, this approximation is not required for the DFPT representation of Eq. (6). It should be noted that only the dipole contribution is considered in Eq. (5) based on the absence of the bulk quadrupole response [48,49] in the H<sub>2</sub>O adsorption monolayer on the metal surface.

The Born effective charge tensor  $Z_{\kappa,\alpha\beta}^*$  is defined as the partial derivative of the polarization  $P_{\alpha}$  with respect to the atomic displacement  $\tau_{\kappa,\beta}$  under a zero electric field:

$$Z_{\kappa,\alpha\beta}^* = \Omega_0 \frac{\partial P_{\alpha}}{\partial \tau_{\kappa,\beta}}. \quad (7)$$

The oscillator strengths  $S_{\alpha\beta,\nu}$  and IR absorption intensity  $\sigma(\omega)$  are easily obtained using  $Z_{\kappa,\alpha\beta}^*$  as

$$S_{\alpha\beta,\nu} = \left( \sum_{\kappa,\alpha'} Z_{\kappa,\alpha\alpha'}^* U_{\nu,\mathbf{q}=0}(\kappa,\alpha') \right) \times \left( \sum_{\kappa,\beta'} Z_{\kappa,\beta\beta'}^* U_{\nu,\mathbf{q}=0}(\kappa,\beta') \right), \quad (8)$$

$$\sigma(\omega) = \sum_{\alpha,\nu} S_{\alpha\alpha,\nu} \delta(\omega - \omega_{\nu}). \quad (9)$$

However, the conventional expression of  $P_{\alpha}$  under the periodic boundary condition (PBC) is unsuitable for a metal/adsorbate system due to the lack of an energy gap [41]. Feibelman *et al.* evaluated the polarization derivative of surface normal direction  $z$  in Eq. (7) from the change in the work function with finite atom displacements and obtained the IR intensity of the H<sub>2</sub>O monolayer on Ru(0001) [50] and Pt(111) [16]. In this study we adopted a slightly different approach; we directly applied a finite electric field and used an alternative representation of the response tensors. Because  $Z_{\kappa,\alpha\beta}^*$  and  $R_{\kappa,\alpha\beta\gamma}$  can be connected to the mixed second- and third-order energy derivatives with respect to atomic displacements and external electric fields, respectively, both quantities can be transferred to the derivative of the Hellman-Feynman force  $F_{\kappa,\alpha}$  with respect to  $\mathcal{E}_{\alpha}$ :

$$Z_{\kappa,\alpha\beta}^* = \frac{\partial F_{\kappa,\beta}}{\partial \mathcal{E}_{\alpha}}, \quad (10)$$

$$R_{\kappa,\alpha\beta\gamma} = \frac{\partial^2 F_{\kappa,\gamma}}{\partial \mathcal{E}_{\alpha} \partial \mathcal{E}_{\beta}}. \quad (11)$$

Using the effective-screening medium (ESM) method [51], a finite electric field  $\mathcal{E}_z$  can be applied along the surface normal direction  $z$ . Then Eqs. (10) and (11) can be evaluated using the finite difference of  $F_{\kappa,\alpha}$  with respect to  $\mathcal{E}_z$ .

To confirm the validity of the above ESM +  $\mathcal{E}$  approach, we evaluated the dipole moment  $\mu_{\alpha}$ , polarizability tensor  $\alpha_{\alpha\beta}$ ,  $Z_{\kappa,\alpha\beta}^*$ , and  $R_{\kappa,\alpha\beta\gamma}$  of an isolated H<sub>2</sub>O molecule using Eqs. (S8), (S9) [23], (10), and (11), respectively. The computational details are described in Sec. S3 [23]. The selected components are listed in Table S2 [23]. Although small differences arise from different functionals, the ESM +  $\mathcal{E}$  results are consistent with previous quantum chemical calculations [38].

### D. Computational details

A four-layer slab of Pt(111) was constructed by cutting fcc crystals. Since the adsorption energy was slightly influenced by the cell parameters suggested by a previous study [52], we fixed the lattice constant of the Pt(111) surface at an experimental value of 3.924 Å. Throughout this study, the Pt atom positions in the first and second bottom layers were fixed in

the crystal positions. We confirmed that the adsorption energy  $E_{\text{ad}}$  obtained for the four-layer slab with two fixed layers was almost the same as that of the six-layer slab with two fixed layers within a few meV/H<sub>2</sub>O. The detailed configurations of the  $\sqrt{39}$  6-ring,  $\sqrt{39}$  5–7-ring, and  $\sqrt{37}$  5–7-ring are shown in Figs. S3(a), S3(b), and S3(c), respectively [23]. The VESTA package was used to visualize the slab and bulk atom coordinates in this study [53]. The cell parameters with the surface parallel directions of the  $\sqrt{3}$ ,  $\sqrt{39}$ , and  $\sqrt{37}$  cells were set to 4.807, 17.332, and 16.882 Å, respectively. The unit-cell lengths along the surface normal direction were set to 25 Å and extended to 30 Å in the absence and presence of a finite electric field, respectively, which provided the correct work function for Pt(111). A previous study showed that the work functions under these conditions and from experiment are 5.77 and 5.9 eV, respectively [54].

To obtain the DFT total energy  $E_{\text{DFT}}$ , the QUANTUM ESPRESSO (QE) code [55,56], a plane-wave basis within the ultrasoft pseudopotential framework [57,58], was used to conduct the spin-unpolarized DFT calculations. The electronic configurations were  $1s^1$  for H,  $2s^2 2p^4$  for O with nonlinear core correction (NLCC) [59], and  $6s^1 6p^0 5d^9$  for Pt with NLCC [60,61]. The cutoff energies were set to 40 and 320 Ry (1 Ry = 13.606 eV) for the wave functions and the augmented charge, respectively, which provided the correct behavior of adsorption and dissociation of H<sub>2</sub>O on oxide surfaces [62]. We also confirmed that the adsorption energy  $E_{\text{ad}}$  obtained by the cutoff energies of 40/320 Ry is almost the same as that of 60/480 Ry within a few meV/H<sub>2</sub>O. In DFT calculations, converged shifted  $k$ -point samplings of  $12 \times 12 \times 1$ ,  $6 \times 6 \times 1$ ,  $4 \times 4 \times 1$ , and  $4 \times 4 \times 1$  were adopted for the  $\sqrt{3}$ ,  $2\sqrt{3}$ ,  $\sqrt{39}$ , and  $\sqrt{37}$  cells, respectively. The electron occupation numbers were determined using the Gaussian smearing technique with a broadening parameter of 0.01 Ry. The atomic positions of H<sub>2</sub>O and Pt were relaxed until the residual forces were less than 0.001 Ry/bohr (1 bohr = 0.52918 Å).

To obtain the phonon frequency  $\omega_{\nu}$  and phonon DOS  $g(\omega)$ , DFPT phonon calculations implemented in QE were applied with the same pseudopotentials, cutoff energies, and cell parameters as those in the DFT calculations. Nonshifted  $k$ -point samplings for electronic states of  $8 \times 8 \times 1$ ,  $1 \times 1 \times 1$ , and  $1 \times 1 \times 1$  were adopted for  $\sqrt{3}$ ,  $\sqrt{39}$ , and  $\sqrt{37}$  cells, respectively. Nonshifted  $q$ -point samplings for phonon modes of  $4 \times 4 \times 1$ ,  $1 \times 1 \times 1$ , and  $1 \times 1 \times 1$  were adopted for the  $\sqrt{3}$ ,  $\sqrt{39}$ , and  $\sqrt{37}$  cells, respectively. In the  $\sqrt{3}$  cell calculation, phonon frequencies obtained on  $q$ -point grids of  $4 \times 4 \times 1$  in reciprocal space were interpolated to dense  $24 \times 24 \times 1$   $q$ -point grids using Fourier interpolation. A self-consistent loop was continued until the residual sum of squares for the response potential was less than  $10^{-14}$  Ry [2]. For the dynamical matrix components, as Pt surface phonon frequencies ( $< 200 \text{ cm}^{-1}$ ) are decoupled from OH vibrational frequencies, only the interatomic force constants of H<sub>2</sub>O were considered, and those of Pt were ignored. Corresponding to this decoupling, the zero-point vibration energy of the pristine Pt(111) slab  $E_{\text{ZPE}}(\text{Pt})$  in Eq. (4) is neglected in this study.

In DFT calculations under a finite electric field using the ESM method, the boundary condition of a metal/vacuum/metal system was used [51]. A self-consistent

loop was continued until the estimated energy error was less than  $10^{-10}$  Ry. In the ESM +  $\mathcal{E}$  method,  $Z_{\kappa,\alpha\beta}^*$  and  $R_{\kappa,\alpha\beta\gamma}$  were obtained using the four- and five-point central-finite-difference formulas to evaluate the first and second derivatives of the DFT forces, respectively. The finite displacement of the electric field was set as 0.005 Ry/e bohr (1 Ry/ebohr = 25.711 V/Å). For the IR intensity in Eq. (9), only the components of the surface normal direction ( $\alpha = z$ ) were used. The Raman intensity was obtained using the representation described in Ref. [63], and only the components of the surface normal direction ( $\alpha = \beta = z$ ) were used. In the phonon DOS, IR intensity, and Raman intensity plots, the  $\delta$  function was replaced by a Gaussian distribution with a standard deviation of  $30 \text{ cm}^{-1}$ . In the second-order nonlinear susceptibility of Eq. (5), the dephasing rate  $\Gamma_{\nu}$  was set to  $30 \text{ cm}^{-1}$ .

### III. RESULTS

#### A. Adsorption structures and energies

Table II shows the calculated adsorption energies  $E_{\text{ad}}$  and surface H<sub>2</sub>O coverage  $n_{\text{H}_2\text{O}}/n_{\text{Pt}}$ , where  $n_{\text{H}_2\text{O}}$  and  $n_{\text{Pt}}$  represent the number of adsorbed H<sub>2</sub>O molecules and top-layer Pt atoms, respectively. In the  $\sqrt{3}$  cell, the PBE and vdW-DF2-B86R functionals showed that  $E_{\text{ad}}$  of the H-down structure was larger than that of H-up, consistent with previous studies [33], whereas the vdW-DF functional showed that  $E_{\text{ad}}$  of the two structures were comparable. Figure 2(a) shows the pair distribution function of the  $\sqrt{3}$  H-down structure, calculated using the PBE functional. The O–O distances were 2.69 and 2.82 Å. This short distance was the same as that in the ice Ih phase. The long distance reflects the incommensurate lattice parameters between the ice Ih and the Pt(111) substrate. The Pt–O distances of H-parallel and H-down H<sub>2</sub>O molecules were 3.07 and 3.28 Å, respectively, which is much longer than that of monomer H<sub>2</sub>O adsorption (2.45 Å, see Table I). The Pt–O distances of H-parallel and H-up molecules were 3.10 and 3.68 Å, respectively (graph is not shown). Similar distance relationships were also observed for the vdW-DF and vdW-DF2-B86R functionals (see Figs. S4(a) and S4(b) [23]). The distances of the  $\sqrt{3}$  H-down structure had a small advantage in terms of the energy gain from H<sub>2</sub>O–H<sub>2</sub>O interactions and Pt – H<sub>2</sub>O interactions on the Pt(111) surface for the PBE functional; however, it is difficult to determine which structure is more stable from the distances, because the small difference in  $E_{\text{ad}}$  easily disappears for other functionals.

Next,  $E_{\text{ad}}$  of the  $\sqrt{39}$  6-ring structure was larger than that of  $\sqrt{3}$  H-down by 10–25 meV/H<sub>2</sub>O in the PBE and vdW-DF2-B86R functionals. Note that the opposite result was obtained using the vdW-DF functional, which might be attributed to the H-down configurations of the  $\sqrt{39}$  6-ring structure. Here we describe the results obtained using only the PBE functional. If we do not mention, similar trends were also observed by the other two functionals (the results of vdW-DF and vdW-DF2-B86R are shown in Figs. S4(c)–S4(f) [23]). The pair distribution function and detailed structure calculated using the PBE functional are shown in Figs. 2(b) and S3(a), respectively. As reported by Meng *et al.* and Feibelman *et al.* [33,34], the partial dissociation of H<sub>2</sub>O molecules was found in the  $\sqrt{39}$  6-ring structure, forming H<sub>3</sub>O and OH groups

TABLE II. Coverages  $n_{\text{H}_2\text{O}}/n_{\text{Pt}}$ , adsorption energies  $E_{\text{ad}}$ , and the heats of adsorption  $H_{\text{ad}}$  of  $\text{H}_2\text{O}$  adsorption structures on Pt(111).

Lattice	Structure	$n_{\text{H}_2\text{O}}/n_{\text{Pt}}$	$E_{\text{ad}}$ [meV/ $\text{H}_2\text{O}$ ]			$H_{\text{ad}}$ [meV/ $\text{H}_2\text{O}$ ]		
			PBE	vdW-DF	vdW-DF2-B86R	PBE	vdW-DF	vdW-DF2-B86R
$\sqrt{3}\times\sqrt{3}$	H-up	2/3	468	508	612			
	H-down		486	502	640	391	400	531
$\sqrt{39}\times\sqrt{39}$	6-ring	32/39	511	476	654			
$\sqrt{39}\times\sqrt{39}$	5-7-ring	28/39	556	529	710	447	403	589
$\sqrt{37}\times\sqrt{37}$		26/37	558	537	709	446	404	605

(while no dissociation was found in the other structures). The dissociation automatically occurred in the relaxation process, which can be attributed to the high  $\text{H}_2\text{O}$  density of the  $\sqrt{39}$  6-ring model. We confirmed that the structure containing two dissociated molecules,  $2(\text{H}_3\text{O} + \text{OH})$ , was more stable than those containing one and three dissociated molecules. We also

confirmed that the structure containing one H-up molecule was more stable than those containing zero or two H-up molecules. From this confirmation, the difference in  $E_{\text{ad}}$  for the H-up/down orientation and  $\text{H}_2\text{O}$  dissociation was within a few meV/ $\text{H}_2\text{O}$ . Reflecting the high  $\text{H}_2\text{O}$  density, the structure has large irregularities in the surface normal direction. Consequently, the  $5\text{H}_2\text{O}$  molecules in the  $\sqrt{39}$  cell were located at Pt-O distances of 2.1–2.3 Å, which are close to the optimized Pt-O distance of the  $\text{H}_2\text{O}$  monomer on Pt(111) compared with that of the  $\sqrt{3}$  H-down structure. It should be noted that the obtained  $\text{H}_2\text{O}$  dissociations may be artificial due to overpacking of  $\text{H}_2\text{O}$  molecules, considering that more stable structures, the  $5\times 7$ -ring structures, do not contain such dissociations. The absence of a dissociated  $\text{H}_2\text{O}$  molecule on Pt(111) is consistent with observed O 1s spectra by high-resolution x-ray photoelectron spectroscopy [64].

Contrary to the 6-ring structure, the  $\sqrt{39}$  5-7-ring structure had highly ordered  $\text{H}_2\text{O}$  configurations, as shown in Fig. S3(b) [23]. In this structure,  $6\text{H}_2\text{O}$  molecules in the  $\sqrt{39}$  cell were located near the surface ( $d_{\text{Pt-O}} = 2.21\text{--}2.25$  Å) and the other molecules were located relatively far from the surface ( $d_{\text{Pt-O}} = 3.3\text{--}4.0$  Å), except for one  $\text{H}_2\text{O}$  molecule ( $d_{\text{Pt-O}} = 2.53$ ). Some structures with various H-up orientations were also examined, and  $E_{\text{ad}}$  decreased with two or more H-up  $\text{H}_2\text{O}$  molecules (there were some structures in which  $E_{\text{ad}}$  did not change with the rotation of one  $\text{H}_2\text{O}$  molecule). This implies that the distant  $\text{H}_2\text{O}$  molecules from the Pt(111) surface tend to orient the H-down configuration, consistent with the experimental results of SFG spectroscopy [18]. In this study, the  $\sqrt{39}$  5-7-ring structure (and the similar  $\sqrt{37}$  structure) had the largest  $E_{\text{ad}}$ ; the 5-7-ring structures maximized the energy gain from the interactions of Pt -  $\text{H}_2\text{O}$  and  $\text{H}_2\text{O}$ - $\text{H}_2\text{O}$ . The pair distribution functions of the  $\sqrt{39}$  5-7-ring structure are shown in Fig. 2(c). Some  $\text{H}_2\text{O}$  molecules had small O-O distance (2.5 Å) that originated from five-member  $\text{H}_2\text{O}$  rings, corresponding to the connection between the anchored  $6\text{H}_2\text{O}$  molecules and the distant  $\text{H}_2\text{O}$  molecules from the surface. It is expected that the frequencies of O-H vibrations are redshifted in such a structure with short O-O bonds [65], as discussed in Sec. III B. It is noted that the redshift can be explained by the effect of internal bond anharmonicity [38].

Table II also lists the heats of adsorption  $H_{\text{ad}}$  of the  $\sqrt{3}$  H-down,  $\sqrt{39}$  5-7-ring, and  $\sqrt{37}$  5-7-ring structures. The zero-point vibration corrections  $\Delta E_{\text{ZPE}}$  of the three structures were -100 to -120 meV/ $\text{H}_2\text{O}$ , obtained from the vibrational (phonon) DOS, as shown in Fig. S5 [23]. Although the OH stretching frequencies of the adsorption structures were redshifted compared to those of an isolated

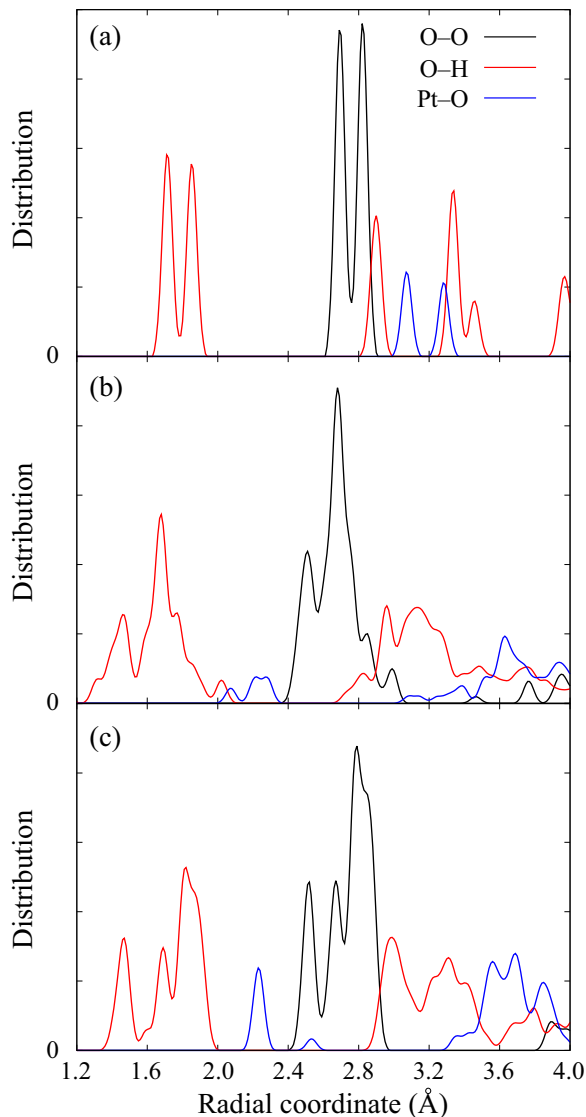


FIG. 2. Pair distribution functions of (a)  $\sqrt{3}$  H-down, (b)  $\sqrt{39}$  6-ring, and (c)  $\sqrt{39}$  5-7-ring structures (PBE functional). The distributions of O-O, O-H, and Pt-O are shown as the black, red, and blue lines, respectively.

$\text{H}_2\text{O}$  molecule, collective modes along the surface parallel directions increased  $E_{\text{ZPE}}$ , resulting in negative values of  $\Delta E_{\text{ZPE}}$ . A previous study reported a comparable  $\Delta E_{\text{ZPE}}$  of the undissociated  $\sqrt{3} \times \sqrt{3}$  structure on the Ru(0001) surface [50]. If we assume that the desorption process of the  $\text{H}_2\text{O}$  monolayer on Pt(111) has a minimal activation barrier, such as a typical physisorption process, the activation energy of the desorption at 0 K can be approximated by  $H_{\text{ad}}$ . Compared with the activation energy of desorption in the experiment, 562 meV/ $\text{H}_2\text{O}$  [13],  $H_{\text{ad}}$  obtained by the PBE, and vdW-DF functionals underestimated the experimental value by 115 and 158 meV, respectively, while that obtained by vdW-DF2-B86R slightly overestimated it by 43 meV. In addition, the wetting condition ( $H_{\text{ad}} > H_{\text{sub}}$ ) was satisfied by vdW-DF2-B86R only; this functional is favorable for describing the thermodynamics of  $\text{H}_2\text{O}$  adsorption monolayer on Pt(111). However, considering the estimated errors of  $H_{\text{sub}}$  in ice Ih (see Table S1 [23]), this agreement could be attributed to the cancellation between the overestimation of the interaction energy of  $\text{H}_2\text{O}-\text{H}_2\text{O}$  and the underestimation of that of Pt- $\text{H}_2\text{O}$  by vdW-DF2-B86R. This implies that the interaction energy of Pt- $\text{H}_2\text{O}$  is underestimated by all three functionals (see Table I). While more accurate functionals are required to satisfy the thermodynamic stability condition of multilayer  $\text{H}_2\text{O}$  on Pt(111), PBE and vdW-DF2-B86R functionals are expected to obtain quantitatively accurate vibrational IR, Raman, and SFG spectra, as shown in the next section.

### B. IR intensity, Raman intensity, and second-order nonlinear susceptibility

It is useful to describe the properties of IR and Raman intensities to interpret the second-order nonlinear susceptibility  $\chi^{(2)}$ , because the value of  $\chi^{(2)}$  is finite only for the IR- and Raman-active modes. Figures 3(a) and S6(a) [23] show the IR intensities of the  $\sqrt{39}$  and  $\sqrt{37}$  5-7-ring structures, respectively. The results of the  $\sqrt{39}$  structure obtained by the PBE functional will be explained, but a similar argument holds for the  $\sqrt{37}$  structure and the vdW-DF2-B86R functional. The stretching modes were located at 1800–3500  $\text{cm}^{-1}$ , while the bending modes were located at lower frequencies. The main components of the displacements  $U_{v,q=0}(\kappa, \alpha)$ , corresponding to  $\omega_v = 3200-3500$  and  $3000-3200 \text{ cm}^{-1}$ , were distributed to the distant  $\text{H}_2\text{O}$  molecules from the surface and the anchored 6 $\text{H}_2\text{O}$  molecules, respectively. In addition, those corresponding to  $\omega_v = 1800-2400 \text{ cm}^{-1}$  were distributed to the connected five-ring  $\text{H}_2\text{O}$  molecules with a short O-O distance (2.5 Å), which was expected from the phenomenological theory [65].

The outline of IR intensity was highly consistent with the previous DFT results reported by Feibelman *et al.* [16]. Overall vibrational frequencies, and the peak intensity ratio of 1600–3500  $\text{cm}^{-1}$ , were also consistent with the experimental IRAS results [16,66]. The IR intensity at 1800–2400  $\text{cm}^{-1}$  was higher than the other intensities in this study; however, the peak intensity at 2000  $\text{cm}^{-1}$  was considerably small in the experiments [16,66]. In DFPT calculations, considering that the main component of  $Z_{\kappa,\alpha\beta}^*$  comes from the surface normal direction ( $\beta = z$ ), the vibrational modes originating from the connected five-ring  $\text{H}_2\text{O}$  molecules have a large

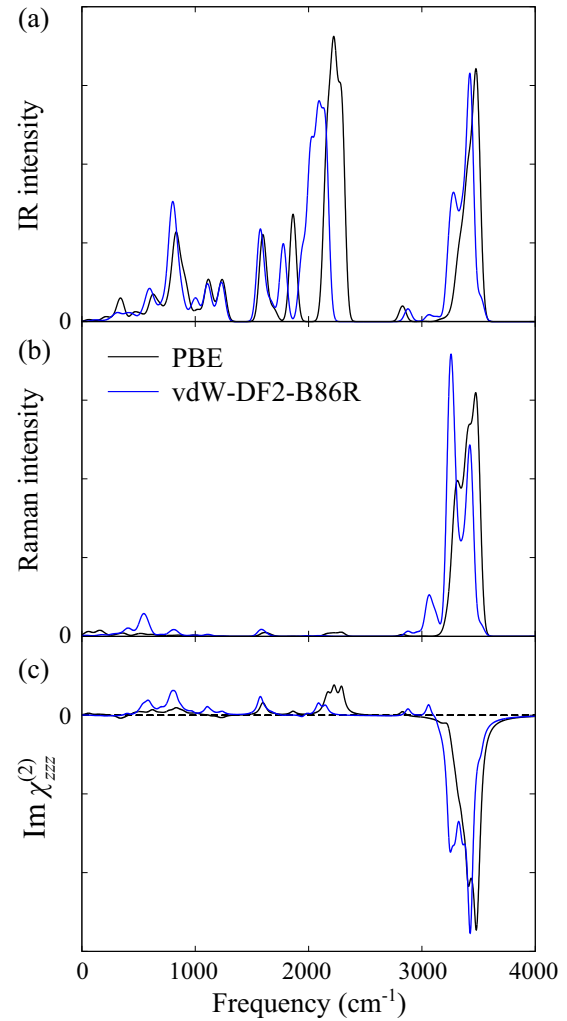


FIG. 3. (a) IR intensities, (b) Raman intensities, and (c) imaginary part of second-order nonlinear susceptibility,  $\text{Im } \chi_{zzz}^{(2)}$ , of the  $\sqrt{39}$  5-7-ring structure. The intensities calculated by PBE and vdW-DF2-B86R functionals are shown as black and blue lines, respectively.

$U_{v,q=0}(\kappa, \alpha)$  in  $\alpha = z$  direction, resulting in relatively large oscillator strengths  $S_{\alpha\alpha,v}$  in Eq. (8). From this argument the calculated intensity at 1800–2400  $\text{cm}^{-1}$  is sensitive to the angles between the surface normal direction and the upward OH directions of the connected five-ring  $\text{H}_2\text{O}$  molecules, with angles ranging from  $58^\circ$  to  $62^\circ$  in the  $\sqrt{39}$  5-7-ring structure. The IR intensity was expected to decrease significantly as the angle approached  $90^\circ$ . However, the origin of the disagreement between the DFT calculations and IRAS experiments remains unclear; this would be a good topic for future study.

Figures 3(b) and S6(b) [23] show the Raman intensities of  $\sqrt{39}$  and  $\sqrt{37}$  5-7-ring structures, respectively. Although the experimental Raman intensity of monolayer  $\text{H}_2\text{O}$  on the Pt(111) surface has not been reported yet, it is expected that the  $x$  and  $y$  components of the transfer coefficients and local field factors are minimal compared with those of the  $z$  component in the  $\text{H}_2\text{O}$  adsorption layer system on Rh(111) and Pt(111) surfaces [67,68]. Thus the calculated results obtained by  $\alpha = \beta = z$  components could capture the characteristics of

the Raman intensity to some extent. The intensities of the stretching modes at high and low frequencies ( $3000\text{--}3500$  and  $1800\text{--}2400\text{cm}^{-1}$ ) were significantly higher than and comparable to those of the bending modes at  $1600\text{cm}^{-1}$ , respectively. The intensity of the bending modes is relatively low, similar to that of the Ice Ih phase [69,70]. The relatively low Raman intensities indicate the high symmetric property of the stretching and bending modes. In addition, the alternative selection rule for IR and Raman spectra [68,71], i.e., high IR and low Raman intensities, holds well at approximately  $1800\text{--}2400\text{cm}^{-1}$ , suggesting that these vibrational modes are composed of in-phase OH collective modes because such collective modes satisfy the above conditions.

The second-order nonlinear susceptibility  $\chi^{(2)}$  behavior is described as follows, with the prospect that only the IR- and Raman-active modes can contribute  $\chi^{(2)}$  spectrum. Figures 3(c) and S6(c) [23] show  $\text{Im } \chi_{zzz}^{(2)}$  of the  $\sqrt{39}$  and  $\sqrt{37}$  5–7-ring structures as a function of IR frequency  $\omega_{\text{IR}}$ , respectively. The peak intensity of  $\text{Im } \chi_{zzz}^{(2)}$  at  $\omega_{\text{IR}} > 3000\text{cm}^{-1}$  was significantly higher than those of the other low-frequency regions. The negative sign of  $\text{Im } \chi_{zzz}^{(2)}$  at  $\omega_{\text{IR}} > 3000\text{cm}^{-1}$  was due to the stretching modes assigned to H-down  $\text{H}_2\text{O}$  molecules, which is consistent with the analyses by the decoupled molecule approximation [10,18,47,67,68]. Although the low-frequency region ( $\omega_{\text{IR}} < 3000\text{cm}^{-1}$ ) has not been observed in experiments thus far, the positive sign of  $\text{Im } \chi_{zzz}^{(2)}$  in that region was predicted. For the stretching modes at  $\omega_{\text{IR}} = 1800\text{--}2400\text{cm}^{-1}$ , the connected five-ring  $\text{H}_2\text{O}$  molecules include H-up  $\text{H}_2\text{O}$  molecules, which results in a positive amplitude. For the bending and libration modes at  $1600$  and  $600\text{--}1200\text{cm}^{-1}$ , respectively, a qualitative one-molecule description can explain the sign of  $\text{Im } \chi_{zzz}^{(2)}$ ; see the discussion in Sec. S4 and Fig. S7 [23]. We briefly describe the real part of  $\chi_{zzz}^{(2)}$  in Fig. S8 (only the results for the PBE functional are displayed) [23]. The sign of  $\text{Re } \chi_{zzz}^{(2)}$  reversed at  $\omega_{\text{IR}} = 3460$ ,  $2170$ , and  $1590\text{cm}^{-1}$ , which corresponds to the peak position of  $\text{Im } \chi_{zzz}^{(2)}$ . Note that we did not account for the nonresonant term  $\chi^{(2)}$  in this study, which can shift the real part value.

The spectra of  $\text{Im } \chi_{zzz}^{(2)}$  calculated with the  $\sqrt{39}$  and  $\sqrt{37}$  5–7-ring structures by vdW-DF2-B86R were compared with those obtained by heterodyne-detected SFG spectroscopy (0.8, 1.4, and 2.6 BL samples,  $1\text{ BL} \approx 1.1 \times 10^{15}\text{ H}_2\text{O}/\text{cm}^2$ ) [10] as shown in Figs. 4(a) and 4(b), respectively. The results obtained using the PBE functional were compared to those obtained using vdW-DF2-B86R, as shown in Fig. S9 [23]. The two functionals give qualitatively similar spectra, so we focus on the vdW-DF2-B86R functional hereafter. Both  $\sqrt{39}$  and  $\sqrt{37}$  spectra show the highest amplitude peaks at  $\omega_{\text{IR}} \sim 3430\text{cm}^{-1}$ , which well reproduced the experimental peak position at  $\sim 3370\text{cm}^{-1}$  of 0.8 and 1.4 BL samples. In addition, the second-highest peaks of the  $\sqrt{39}$  and  $\sqrt{37}$  structures at approximately  $3250\text{cm}^{-1}$  are consistent with the peak positions at  $3300$  and  $3290\text{cm}^{-1}$  for 0.8 and 1.4 BL, respectively. The negative amplitude of the second-highest peak of the  $\sqrt{39}$  structure was larger than that of the  $\sqrt{37}$  structures. With an increase in the number of  $\text{H}_2\text{O}$  layers, a similar increase in the negative amplitude was observed in the experiment; the experimental peak at  $3280\text{cm}^{-1}$  of 2.6 BL can be attributed to the OH stretching mode in the bulky

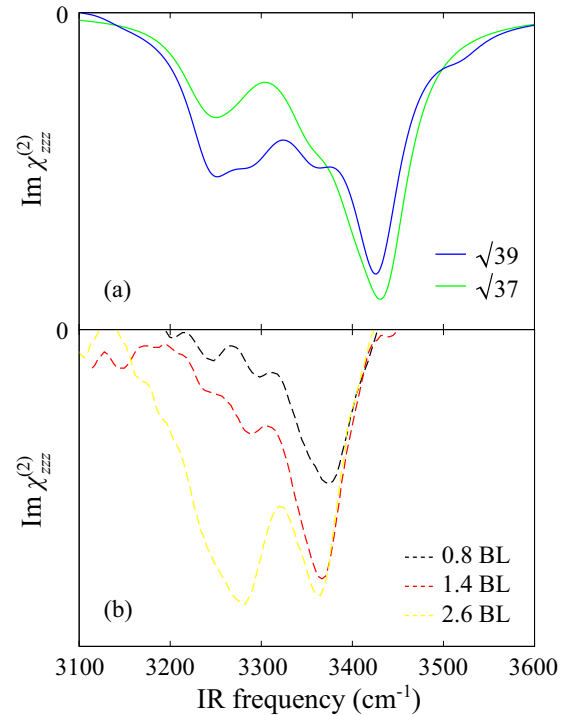


FIG. 4.  $\text{Im } \chi_{zzz}^{(2)}$  as a function of IR frequency  $\omega_{\text{IR}}$ . (a) Spectra of the  $\sqrt{39}$  and  $\sqrt{37}$  5–7-ring structures calculated using the vdW-DF2-B86R functional are shown as blue and green lines, respectively. (b) Experimental spectra of 0.8, 1.4, and 2.6 BL from Ref. [10] are shown as black, red, and yellow dotted lines, respectively.

upper layers. Therefore it is interesting to determine which vibrational molecules contribute to the increase in the negative amplitude. Figures S10(a) and S10(b) [23] show the vibrational (phonon) DOSs of  $\sqrt{39}$  and  $\sqrt{37}$  5–7-ring structures, respectively, projected onto three types of  $\text{H}_2\text{O}$  molecules: the center six-ring, the upper five-ring, and the other six- and seven-ring  $\text{H}_2\text{O}$  molecules, as indicated in Figs. S10(c) and S10(d) [23]. The DOSs of the two structures at  $3250\text{cm}^{-1}$  are entirely composed of the five-ring and six- and seven-ring  $\text{H}_2\text{O}$  molecules, and that of the  $\sqrt{39}$  structure is slightly larger than that of the  $\sqrt{37}$  structure because of additional two  $\text{H}_2\text{O}$  molecules belonging to the six- and seven-ring. From the above discussion, the method developed in this study is useful for attributing the peak of  $\chi^{(2)}$  spectral to characteristic modes and atoms.

#### IV. CONCLUSIONS

We investigated the system of adsorbed  $\text{H}_2\text{O}$  monolayer on the Pt(111) surface using DFT and DFPT calculations. The adsorption energies  $E_{\text{ad}}$  of  $\sqrt{3}$  H-up/H-down,  $\sqrt{39}$  6-ring,  $\sqrt{39}$  5–7-ring, and  $\sqrt{37}$  5–7-ring structures were obtained by employing the PBE, vdW-DF, and vdW-DF2-B86R functionals. The atom pair distribution functions indicated that the highly ordered 5–7-ring structures, which contained anchored and distinct  $\text{H}_2\text{O}$  molecules on the Pt(111) surface, maximized the interaction energies of Pt– $\text{H}_2\text{O}$  and  $\text{H}_2\text{O}$ – $\text{H}_2\text{O}$ . We further included zero-point vibration correction and estimated the heats of adsorption  $H_{\text{ad}}$  of  $\sqrt{3}$

H-down,  $\sqrt{39}$  5–7-ring, and  $\sqrt{37}$  5–7-ring structures, which indicated that  $H_{\text{ad}}$  obtained by vdW-DF2-B86R was in good agreement with the activation energy of desorption in the experiment. However, those of the PBE and vdW-DF functionals were underestimated. In addition to the IR and Raman intensities, the second-order nonlinear susceptibility  $\chi_{zzz}^{(2)}$  was obtained by applying the DFPT formulation combined with the  $\text{ESM} + \mathcal{E}$  approach. The IR intensity of the  $\sqrt{39}$  5–7-ring structure was consistent with that of the IRAS experiments, except for the relatively high intensity at 1800–2400  $\text{cm}^{-1}$ . In the same structure, the negative and positive signs of  $\text{Im } \chi_{zzz}^{(2)}$  were obtained in the high (3000–3500  $\text{cm}^{-1}$ ) and low (600–2400  $\text{cm}^{-1}$ ) frequency regions, respectively. Finally, the spectra of  $\text{Im } \chi_{zzz}^{(2)}$  calculated with the  $\sqrt{39}$  and  $\sqrt{37}$  5–7-ring structures were consistent with those obtained by heterodyne-detected SFG spectroscopy. The peaks of the  $\sqrt{39}$  and  $\sqrt{37}$  structures at approximately 3250  $\text{cm}^{-1}$  are composed of the OH stretching of the upper five-ring and six- and seven-ring  $\text{H}_2\text{O}$  molecules. This study paves the way for understanding the properties of metal-adsorbed water

systems and electrochemical interfacial systems using SFG spectroscopy.

The supporting data for this article (the raw data of optimized structures) are openly available from the ISSP data repository [72].

#### ACKNOWLEDGMENTS

This work was supported in part by MEXT as the “Program for Promoting Research on the Supercomputer Fugaku” (Fugaku Battery & Fuel Cell Project, Grant No. JPMXP1020200301), by JSPS as Grants in Aid for Scientific Research on Innovative Area “Hydrogenomics” (Grant No. 18H05519), by JSPS KAKENHI (Grants No. JP20K15376 and No. 22H00296), and by JST-PRESTO (Grant No. JP-MJPR1907). The calculations were performed with the facilities of the Supercomputer Center, The Institute for Solid State Physics, The University of Tokyo, and the Fujitsu PRIMERGY CX400M1/CX2550M5 (Oakbridge-CX) in the Information Technology Center, The University of Tokyo.

- [1] J. O’M. Bockris and A. K. N. Reddy, *Modern Electrochemistry* (Plenum, New York, 1973).
- [2] A. J. Bard and L. R. Faulkner, *Electrochemical Methods: Fundamentals and Applications* (Wiley, New York, 1980).
- [3] A. Groß and S. Sakong, *Ab initio* simulations of water/metal interface, *Chem. Rev.* **122**, 10746 (2022).
- [4] N. Markovic and P. Ross Jr., Surface science studies of model fuel cell electrocatalysts, *Surf. Sci. Rep.* **45**, 117 (2002).
- [5] M. Otani, I. Hamada, O. Sugino, Y. Morikawa, Y. Okamoto, and T. Ikeshoji, Electrode dynamics from first principles, *J. Phys. Soc. Jpn.* **77**, 024802 (2008).
- [6] J. Lan, V. V. Rybkin, and M. Iannuzzi, Ionization of water as an effect of quantum delocalization at aqueous electrode interfaces, *J. Phys. Chem. Lett.* **11**, 3724 (2020).
- [7] N. Materer, U. Starke, A. Barbieri, M. A. Van Hove, G. A. Somorjai, G.-J. Kroes, and C. Minot, Molecular surface structure of a low-temperature ice Ih(0001) crystal, *J. Chem. Phys.* **99**, 6267 (1995).
- [8] A. Hodgson and S. Haq, Water adsorption and the wetting of metal surfaces, *Surf. Sci. Rep.* **64**, 381 (2009).
- [9] J. Carrasco, A. Hodgson, and A. Michaelides, A molecular perspective of water at metal interfaces, *Nat. Mater.* **11**, 667 (2012).
- [10] T. Sugimoto and Y. Matsumoto, Orientational ordering in heteroepitaxial water ice on metal surfaces, *Phys. Chem. Chem. Phys.* **22**, 16453 (2020).
- [11] A. Glebov, A. P. Graham, A. Menzel, and J. P. Toennies, Orientational ordering of two-dimensional ice on Pt(111), *J. Chem. Phys.* **106**, 9382 (1997).
- [12] S. Haq, J. Harnett, and A. Hodgson, Growth of thin crystalline ice films on Pt(111), *Surf. Sci.* **505**, 171 (2002).
- [13] J. L. Daschbach, B. M. Peden, R. S. Smith, and B. D. Kay, Adsorption, desorption, and clustering of  $\text{H}_2\text{O}$  on Pt(111), *J. Chem. Phys.* **120**, 1516 (2004).
- [14] S. Nie, P. J. Feibelman, N. C. Bartelt, and K. Thümer, Pentagons and heptagons in the first water layer on Pt(111), *Phys. Rev. Lett.* **105**, 026102 (2010).
- [15] P. J. Feibelman, N. C. Bartelt, S. Nie, and K. Thümer, Interpretation of high-resolution images of the best-bound wetting layers on Pt(111), *J. Chem. Phys.* **133**, 154703 (2010).
- [16] P. J. Feibelman, G. A. Kimmel, R. S. Smith, N. G. Petrik, T. Zubkov, and B. D. Kay, A unique vibrational signature of rotated water monolayers on Pt(111): Predicted and observed, *J. Chem. Phys.* **134**, 204702 (2011).
- [17] X. Su, L. Lianos, Y. R. Shen, and G. A. Somorjai, Surface-induced ferroelectric ice on Pt(111), *Phys. Rev. Lett.* **80**, 1533 (1998).
- [18] T. Sugimoto, N. Aiga, Y. Otsuki, K. Watanabe, and Y. Matsumoto, Emergent high- $T_c$  ferroelectric ordering of strongly correlated and frustrated protons in a heteroepitaxial ice film, *Nat. Phys.* **12**, 1063 (2016).
- [19] Y. Otsuki, K. Watanabe, T. Sugimoto, and Y. Matsumoto, Enhanced structural disorder at a nanocrystalline ice surface, *Phys. Chem. Chem. Phys.* **21**, 20442 (2019).
- [20] D. R. Hamann,  $\text{H}_2\text{O}$  hydrogen bonding in density-functional theory, *Phys. Rev. B* **55**, R10157 (1997).
- [21] P. J. Feibelman, Lattice match in density functional calculations: Ice Ih *vs.*  $\beta$ -AgI, *Phys. Chem. Chem. Phys.* **10**, 4688 (2008).
- [22] I. Hamada, A van der Waals density functional study of ice Ih, *J. Chem. Phys.* **133**, 214503 (2010).
- [23] See Supplemental Material at <http://link.aps.org/supplemental/10.1103/PhysRevMaterials.7.115803> for the computational details for ice Ih phase; finite-temperature vibrational contributions; the computational details of an isolated  $\text{H}_2\text{O}$  molecule under an electric field; the adsorption layer structures of Pt(111)/ $\text{H}_2\text{O}$ ; the pair distribution functions of adsorption structures; the DOS of vibrational modes of adsorption structures; the IR and Raman intensities, and imaginary part of second-order nonlinear susceptibility of  $\sqrt{37}$  5–7-ring structure; the  $\text{H}_2\text{O}$  molecule description of bending and libration motions; and the second-order nonlinear susceptibility and vibrational DOSs of  $\sqrt{39}$  and  $\sqrt{37}$  5–7-ring structures. The Supplemental Material also contains Refs. [24,25].

- [24] V. R. Brill and A. Tippe, Gitterparameter von eis i bei tiefen temperaturen, *Acta Cryst.* **23**, 343 (1967).
- [25] E. Whalley, The difference in the intermolecular forces of H<sub>2</sub>O and D<sub>2</sub>O, *Trans. Faraday Soc.* **53**, 1578 (1957).
- [26] J. P. Perdew, K. Burke, and M. Ernzerhof, Generalized gradient approximation made simple, *Phys. Rev. Lett.* **77**, 3865 (1996).
- [27] M. Dion, H. Rydberg, E. Schröder, D. C. Langreth, and B. I. Lundqvist, Van der Waals density functional for general geometries, *Phys. Rev. Lett.* **92**, 246401 (2004).
- [28] I. Hamada, van der Waals density functional made accurate, *Phys. Rev. B* **89**, 121103(R) (2014).
- [29] D. D. Wagman, W. H. Evans, V. B. Parker, R. H. Schumm, I. Halow, S. M. Bailey, K. L. Churney, and R. L. Nuttall, The NBS tables of chemical thermodynamic properties, Selected values for inorganic and C1 and C2 organic substances in SI units, *J. Phys. Chem. Ref. Data* **11**, Suppl. 2 (1982).
- [30] I. Hamada, K. Lee, and Y. Morikawa, Interaction of water with a metal surface: Importance of van der Waals forces, *Phys. Rev. B* **81**, 115452 (2010).
- [31] J. Carrasco, B. Santra, J. Klimeš, and A. Michaelides, To wet or not to wet? Dispersion forces tip the balance for water ice on metals, *Phys. Rev. Lett.* **106**, 026101 (2011).
- [32] J. Carrasco, J. Klimeš, and A. Michaelides, The role of van der Waals forces in water adsorption on metals, *J. Chem. Phys.* **138**, 024708 (2013).
- [33] S. Meng, E. G. Wang, and S. Gao, Water adsorption on metal surfaces: A general picture from density functional theory studies, *Phys. Rev. B* **69**, 195404 (2004).
- [34] P. J. Feibelman, Comment on “Vibrational recognition of hydrogen-bonded water networks on a metal surface,” *Phys. Rev. Lett.* **91**, 059601 (2003).
- [35] J. Haruyama, S. Takagi, K. Shimoda, I. Watanabe, K. Sodeyama, T. Ikeshoji, and M. Otani, Thermodynamic analysis of Li-intercalated graphite by first-principles calculations with vibrational and configurational contributions, *J. Phys. Chem. C* **125**, 27891 (2021).
- [36] Y. R. Shen, *Principle of Nonlinear Optics* (Wiley, New York, 1984).
- [37] X. Wei, P. B. Miranda, C. Zhang, and Y. R. Shen, Sum-frequency spectroscopic studies of ice interfaces, *Phys. Rev. B* **66**, 085401 (2002).
- [38] A. Morita and J. T. Hynes, A theoretical analysis of the sum frequency generation spectrum of the water surface, *Chem. Phys.* **258**, 371 (2000).
- [39] A. Morita and J. T. Hynes, A theoretical analysis of the sum frequency generation spectrum of the water surface. II. Time-dependent approach, *J. Phys. Chem. B* **106**, 673 (2002).
- [40] X. Gonze and C. Lee, Dynamical matrices, Born effective charges, dielectric permittivity tensors, and interatomic force constants from density-functional perturbation theory, *Phys. Rev. B* **55**, 10355 (1997).
- [41] S. Baroni, S. de Gironcoli, A. Dal Corso, and P. Giannozzi, Phonons and related crystal properties from density-functional perturbation theory, *Rev. Mod. Phys.* **73**, 515 (2001).
- [42] S. Baroni and R. Resta, *Ab initio* calculation of the low-frequency Raman cross section in silicon, *Phys. Rev. B* **33**, 5969 (1986).
- [43] P. Umari, A. Pasquarello, and A. Dal Corso, Raman scattering intensities in  $\alpha$ -quartz: A first-principles investigation, *Phys. Rev. B* **63**, 094305 (2001).
- [44] M. Lazzeri and F. Mauri, First-principles calculation of vibrational Raman spectra in large systems: Signature of small rings in crystalline SiO<sub>2</sub>, *Phys. Rev. Lett.* **90**, 036401 (2003).
- [45] T. Ishiyama and A. Morita, Analysis of anisotropic local field in sum frequency generation spectroscopy with the charge response kernel water model, *J. Chem. Phys.* **131**, 244714 (2009).
- [46] T. Ohto, K. Usui, T. Hasegawa, M. Bonn, and Y. Nagata, Toward *ab initio* molecular dynamics modeling for sum-frequency generation spectra: An efficient algorithm based on surface-specific velocity-velocity correlation function, *J. Chem. Phys.* **143**, 124702 (2015).
- [47] T. Sugimoto, Y. Otsuki, T. Ishiyama, A. Morita, K. Watanabe, and Y. Matsumoto, Topologically disordered mesophase at the topmost surface layer of crystalline ice between 120 and 200 K, *Phys. Rev. B* **99**, 121402(R) (2019).
- [48] K. Shiratori and A. Morita, Theory of quadrupole contributions from interface and bulk in second-order optical processes, *Bull. Chem. Soc. Jpn.* **85**, 1061 (2012).
- [49] Q. Wan and G. Galli, First-principles framework to compute sum-frequency generation vibrational spectra of semiconductors and insulators, *Phys. Rev. Lett.* **115**, 246404 (2015).
- [50] P. J. Feibelman, Vibrations of a water adlayer on Ru(0001), *Phys. Rev. B* **67**, 035420 (2003).
- [51] M. Otani and O. Sugino, First-principles calculations of charged surfaces and interfaces: A plane-wave nonrepeated slab approach, *Phys. Rev. B* **73**, 115407 (2006).
- [52] L. Yan, Y. Sun, Y. Yamamoto, S. Kasamatsu, I. Hamada, and O. Sugino, Hydrogen adsorption on Pt(111) revisited from random phase approximation, *J. Chem. Phys.* **149**, 164702 (2018).
- [53] K. Momma and F. Izumi, *VESTA 3* for three-dimensional visualization of crystal, volumetric and morphology data, *J. Appl. Crystallogr.* **44**, 1272 (2011).
- [54] J. Haruyama, T. Ikeshoji, and M. Otani, Electrode potential from density functional theory calculations combined with implicit solvation theory, *Phys. Rev. Mater.* **2**, 095801 (2018).
- [55] P. Giannozzi, S. Baroni, N. Bonini, M. Calandra, R. Car, C. Cavazzoni, D. Ceresoli, G. L. Chiarotti, M. Cococcioni, I. Dabo *et al.*, QUANTUM ESPRESSO: A modular and open-source software project for quantum simulations of materials, *J. Phys.: Condens. Matter* **21**, 395502 (2009).
- [56] P. Giannozzi, O. Andreussi, T. Brumme, O. Bunau, M. B. Nardelli, M. Calandra, R. Car, C. Cavazzoni, D. Ceresoli, M. Cococcioni *et al.*, Advanced capabilities for materials modeling with QUANTUM ESPRESSO, *J. Phys.: Condens. Matter* **29**, 465901 (2017).
- [57] D. Vanderbilt, Soft self-consistent pseudopotentials in a generalized eigenvalue formalism, *Phys. Rev. B* **41**, 7892 (1990).
- [58] A. M. Rappe, K. M. Rabe, E. Kaxiras, and J. Joannopoulos, Optimized pseudopotentials, *Phys. Rev. B* **41**, 1227 (1990).
- [59] S. G. Louie, S. Froyen, and M. L. Cohen, Nonlinear ionic pseudopotentials in spin-density-functional calculations, *Phys. Rev. B* **26**, 1738 (1982).
- [60] A. Dal Corso, Pseudopotentials periodic table: From H to Pu, *Comput. Mater. Sci.* **95**, 337 (2014).
- [61] A Library of Ultrasoft and PAW Pseudopotentials, <https://dalcorso.github.io/pslibrary/> (Accessed: November 2, 2023).
- [62] S. Muhammadiyah, J. Haruyama, S. Kasamatsu, and O. Sugino, Effect of nitrogen doping and oxygen vacancy on the oxygen reduction reaction on the tetragonal zirconia(101) surface, *J. Phys. Chem. C* **126**, 15662 (2022).

- [63] D. Porezag and M. R. Pederson, Infrared intensities and Raman-scattering activities within density-functional theory, *Phys. Rev. B* **54**, 7830 (1996).
- [64] A. Shavorskiy, M. J. Gladys, and G. Held, Chemical composition and reactivity of water on hexagonal Pt-group metal surfaces, *Phys. Chem. Chem. Phys.* **10**, 6150 (2008).
- [65] P. A. Thiel and T. E. Madey, The interaction of water with solid surfaces: Fundamental aspects, *Surf. Sci. Rep.* **7**, 211 (1987).
- [66] K. Harada, T. Sugimoto, F. Kato, K. Watanabe, and Y. Matsumoto, Thickness dependent homogeneous crystallization of ultrathin amorphous solid water films, *Phys. Chem. Chem. Phys.* **22**, 1963 (2020).
- [67] Y. Otsuki, T. Sugimoto, T. Ishiyama, A. Morita, K. Watanabe, and Y. Matsumoto, Unveiling subsurface hydrogen-bond structure of hexagonal water ice, *Phys. Rev. B* **96**, 115405 (2017).
- [68] N. Aiga, T. Sugimoto, Y. Otsuki, K. Watanabe, and Y. Matsumoto, Origins of emergent high- $T_c$  ferroelectric ordering in heteroepitaxial ice films: Sum-frequency generation vibrational spectroscopy of H<sub>2</sub>O and D<sub>2</sub>O ice films on Pt(111), *Phys. Rev. B* **97**, 075410 (2018).
- [69] T. Shigenari and K. Abe, Vibrational modes of hydrogens in the proton ordered phase XI of ice: Raman spectra above 400 cm<sup>-1</sup>, *J. Chem. Phys.* **136**, 174504 (2012).
- [70] Y. Liu and L. Ojamäe, Raman and IR spectra of Ice Ih and Ice XI with an assessment of DFT methods, *J. Phys. Chem. B* **120**, 11043 (2016).
- [71] M. J. Wójcik, K. Szczeponek, and S. Ikeda, Theoretical study of the OH/OD stretching regions of the vibrational spectra of ice Ih, *J. Chem. Phys.* **117**, 9850 (2002).
- [72] [https://isspns-gitlab.issp.u-tokyo.ac.jp/j-haruyama/Pt111\\_H2O-monolayer](https://isspns-gitlab.issp.u-tokyo.ac.jp/j-haruyama/Pt111_H2O-monolayer) (Accessed: November 2, 2023).